Materials & Design 224 (2022) 111275

Contents lists available at ScienceDirect

Materials & Design

journal homepage: www.elsevier.com/locate/matdes

Water flow through bone: Neutron tomography reveals differences in water permeability between osteocytic and anosteocytic bone material

Andreia Silveira [a], Nikolay Kardjilov [b], Henning Markötter [c], Elena Longo [d,e], Imke Greving [d], Peter Lasch [f], Ron Shahar [g], Paul Zaslansky [a,*]

[a] Department for Operative, Preventive and Pediatric Dentistry, Charité -Universitaetsmedizin, 14197 Berlin, Germany
[b] Institute of Applied Materials, Helmholtz Center for Materials and Energy, 14109 Berlin, Germany
[c] Bundesanstalt für Materialforschung und - Prüfung (BAM), 12489 Berlin, Germany
[d] Institute of Materials Physics, Helmholtz-Zentrum Hereon, 21502 Geesthacht, Germany
[e] Elettra – Sincrotrone Trieste S. C. p. A., 34149 Trieste, Italy
[f] Centre for Biological Threats and Special Pathogens, Proteomics and Spectroscopy, (ZBS6), Robert Koch-Institute, 13353 Berlin, Germany
[g] Koret School of Veterinary Medicine, The Robert H. Smith Faculty of Agriculture, Food and Environmental Sciences, Hebrew University of Jerusalem, 7610001 Rehovot, Israel

HIGHLIGHTS

- Anosteocytic bone material is more water permeable than osteocytic bone material.
- In osteocytic zebrafish bone, water flow appears to be confined to the lacunar-canalicular network.
- Anosteocytic medaka bone is water permeable and containes far less proteoglycans.
- 3D correlation of neutron and X-ray tomographies with micron resolution reveals water diffusion across the bone matrix.

GRAPHICAL ABSTRACT

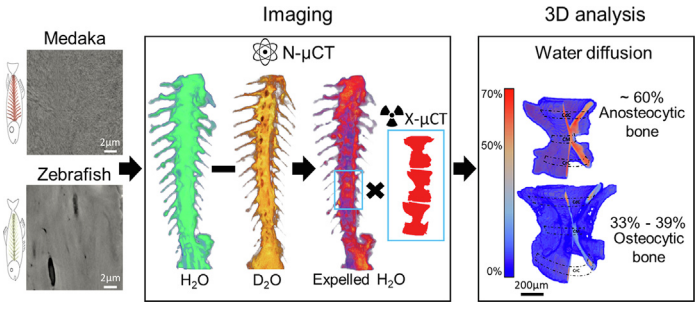

ARTICLE INFO

Article history:
Received 6 July 2022
Revised 3 October 2022
Accepted 19 October 2022
Available online 20 October 2022

Keywords:
Bone porosity
Anosteocytic bone
Water permeability
Neutron tomography
Proteoglycans

ABSTRACT

Vertebrate bones are made of a nanocomposite consisting of water, mineral and organics. Water helps bone material withstand mechanical stress and participates in sensation of external loads. Water diffusion across vertebrae of medaka (bone material lacking osteocytes) and zebrafish (bone material containing osteocytes) was compared using neutron tomography. Samples were measured both wet and following immersion in deuterated-water (D_2O). By quantifying H^+ exchange and mutual alignment with X-ray μCT scans, the amount of water expelled from complete vertebra was determined. The findings revealed that anosteocytic bone material is almost twice as amenable to D_2O diffusion and H_2O exchange, and that unexpectedly, far more water is retained in osteocytic zebrafish bone. Diffusion in osteocytic bones (only 33 % – 39 % water expelled) is therefore restricted as compared to anosteocytic bone (~ 60 % of water expelled), presumably because water flow is confined to the lacunar-canalicular network (LCN) open-pore system. Histology and Raman spectroscopy showed that anosteocytic bone contains less proteoglycans than osteocytic bone. These findings identify a previously unknown functional difference

Abbreviations: CdC, Caudal cone; Cm, Centrum middle; CrC, Cranial cone; D_2O, Deuterated-water; ECM, Extracellular matrix; GAGs, Glycosaminoglycans; H_2O, Water; LCN, Lacunar-canalicular network; N-μCT, Neutron tomography; PGs, Proteoglycans; μCT, Micro-computed X-ray tomography.

* Corresponding author.
E-mail address: paul.zaslansky@charite.de (P. Zaslansky).

https://doi.org/10.1016/j.matdes.2022.111275

between the two bone materials. Therefore, this study proposes that osteocytic bone retains water, aided by non-collagenous proteins, which contribute to its poroelastic mechano-transduction of water flow confined inside the LCN porosity.

1. Introduction

Bones are made of a porous biocomposite with a hierarchical structure that has been well documented [1–3]. The material bone comprises nanofibers of collagen type I embedded in and surrounding nanoparticles of carbonated hydroxyapatite as well as non-collagenous proteins (γ-carboxyglutamate-containing proteins, proteoglycans (PGs) and glycoproteins) [1,4,5]. Bone also contains appreciable amounts of water reportedly up to ~20 % of the total volume [6,7]. Collectively these ingredients establish the mineralized collagen fibril extracellular matrix (ECM), a three-dimensional (3D) structure that provides bones with rigidity, elasticity, and toughness that are important for their lifelong functions in the skeleton [8]. One important aspect of this 3D structure is the accommodation of an intricate open porosity spanning the micro to nanometer length-scales [9,10]. The nanometer sized hydroxyapatite crystals confer stiffness and compressive strength, whereas the organic matrix is a major contributor to bone toughness and tensile strength [11]. PGs in the ECM contain glycosaminoglycans (GAGs) that attract water to the bone matrix due to their high negative charges and consequently they influence the tissue-level mechanical properties [12–15]. The presence of water modulates the response to load, acting as a plasticizer and enhancing strain energy distribution, thus significantly increasing bone toughness [16]. Therefore, each component of the composite is important for the long-term mechanical function of the skeleton.

The open porosity of bony tissues makes it possible for water to exchange with the environment, which is important for the normal physiology of bones. The literature describes water in bone as being free, loosely bound, tightly bound, and structural [17–20]. Free water occupies the larger chambers, most notably the lacunar-canalicular network (LCN), internal porosity comprising micrometer-sized embedded osteocytes cells that are connected with sub-micrometer canaliculi channels, where fluid flows according to pressure gradients [18,21]. Loosely bound water wets and adheres to exposed surfaces, possibly by single hydrogen bonds [22]. Tightly bound water is associated with triple and double hydrogen bonding e.g. between collagen molecules in the matrix, surrounding bone cavities [22–24]. Structural water is embedded within the nanostructures, for example within apatite nanocrystals [25,26]. Indeed, far more energy is needed to remove structural water than is needed to expel free water from inside the voids in the bone matrix [24]. Water removal from bone has been described by thermal and solvent dehydration techniques [16,27,28,29,30]. But it is not know to what extent the bone matrix itself is watertight, e.g. if diffusion through the ECM takes place under ambient conditions, or if water can seep out of internal cavities.

Water flow within the LCN open porosity is well described and is thought to have several complementary biological and mechanical functions [18,31,32,33,34]. It transports nutrients and waste products required or produced by osteocytes within the lacunae of the bone matrix. Both inward and outward flow is needed to sustain bone vitality [35,36]. Water flow is believed to have a role in bone remodeling, a process in which newly laid down material replaces resorbed ECM tissue. This process is typical for turnover in osteocytic bony tissues in which micro-damage has accumulated [37,38,32,39]. The remodeling process is believed to be regulated by the osteocytes that also react to physical deformation cues. Biochemical signals activated by mechanotransduction stimulate bone deposition or resorption, though the exact mechanism by which bone cells translate the mechanical response is so far not fully established. According to some bone poroelasticity models, the most likely conduction mechanism for delivering deformation information across the bone matrix is fluid flow through the LCN [9,40]. Studies suggest that the flow of interstitial fluid deforms osteocytes within the bone matrix. This in turn, induces shear stresses that lead to deformation of actin filaments in the osteocyte cytoskeleton [36,32,41]. The osteocytes then activate biochemical signals that orchestrate the processes of bone remodeling. Though consensus exists that fluid is essential for the physiological and mechanical performance of bone, the manner by which pressurization and pressure-gradients are delivered is not fully known. Indeed, any such pressure would certainly require the bone to be impermeable so that water flow is confined to the immediate surroundings of the embedded cells [40].

The relationship between LCN geometry and fluid flow through the network is a subject of ongoing research [42]. To that end, it is important to understand how permeable or water-tight the ECM matrix surrounding the LCN open porosity actually is. The lacunar-canalicular open porosity consists of < 10 μm sized voids interconnected by sub-micrometer diameter canaliculi channels [43–45]. Bone also has interconnected nanoporosity within the mineralized matrix, as shown recently by Tang et al. [10], who demonstrated the existence of nano channels (10 – 50 nm) within the ECM. Porosity therefore spans three orders of magnitude, ensuring liquid transport through bone. To date however, there have not been many studies directly revealing water flow within the bone matrix itself. In fact, to examine the permeability of ECM, there is a need to compare similar bones with and without LCN porosity, which has so far never been reported.

Zebrafish (*Danio rerio*) and medaka (*Oryzias latipes*) are valuable *in vivo* fish models often used to study skeletal development, bone disorders, and drug effects. Both species are similar in size, anatomy, habitat, and ecology and they exhibit substantial physiological homology to mammals, including humans. Moreover, their rapid development and short reproduction cycles have made them frequently used animal models [46]. But they have different evolutionary records and important structural differences. Zebrafish bone has a LCN structure similar to mammalian bone, as it is osteocytic, with physiologically active osteocytes entrapped within lacunae and connected with neighboring cells in the bone matrix by a canalicular network [47,48]. Similar to mammalian bone, water in zebrafish is found in two compartments: the LCN porosity, and the bone ECM composite. On the other hand, the bones of medaka lack osteocytes. In such bones, water can only reside in the ECM [47–50]. The absence of osteocytes in the bones of medaka (hence anosteocytic bone) makes them interesting animal models for investigating alternative responses of bone material to deformation and the putative relationship between tissue remodeling and poroelasticity models. Specifically, a recent study demonstrated that the bone material in vertebrae of medaka and zebrafish is comparable, with similar characteristics, mineral content, structure arrangement, and mechanical behavior. The authors

reported that the main difference is the morphologically visible lack of the LCN in medaka bone [47]. The lack of an LCN compartment in medaka suggests that the water content of this bone should be lower and less mobile than in zebrafish, although this has never been demonstrated.

Bone scatters light, therefore it is not easy to observe and measure water flow across the extracellular matrix. Nuclear magnetic resonance (NMR) studies have reveled water flow in bone but on a very local, atomic length scale. In fact, several irradiative methods are able to reveal fluid flow in bone. These include Raman spectroscopy, Near Infrared Spectroscopic and NMR imaging techniques. They have all been used to estimate bone permeability and fluid flow [17,24,30,51,52,53,54]. However, none of these techniques can directly reveal how much water diffuses through the LCN porosity of entire bones. Therefore, we employed a technique that can directly evaluate water diffusion in 3D. Neutron radiography is less-known, yet it is a well established non-destructive imaging method that relies on strong scattering interactions between incoming neutrons and hydrogen (H) nuclei [55–57]. Importantly, this method is very sensitive to changes in hydrogen content [58], and despite moderate spatial-resolution (>5 μm), it is able to detect water layers down to 1 μm. Although neutron imaging techniques have frequently been used to study the fluid distribution in rocks, soils, and concrete, relatively little is known about their possible application to assess bone permeability. When combined with rotation geometries, neutron radiographies can be reconstructed to provide 3D distributions of water. Such information is complementary to density obtained by laboratory micro-computed X-ray tomography (μCT) because the X-ray absorbing apatite mineral of bone is largely transparent to neutrons. Thus, for 3D characterization of bone, combining neutrons and X-ray-based microtomography is crucial to study relations between hydration and the mineralized component of the bone ECM.

This work presents new insights into water permeability differences between osteocytic bone of zebrafish and anosteocytic bone of medaka. Neutron tomography is used initially to image H_2O saturated samples and thereafter compare the same samples following immersion in D_2O. Consequently, it is possible to follow ambient changes in hydrogen concentration, corresponding to changes in water distribution. We show for the first time the effects of water exchange in 3D within the matrix of similar-sized fish vertebra, directly comparing bones with and without an inbuilt LCN open pore system.

2. Materials and methods

2.1. Samples

Nine adult medaka and ten adult zebrafish were used for the study. All the experiments were approved by the ethics committee of the Hebrew University of Jerusalem. The vertebral column of each fish, that was cryopreserved at − 80 °C, was carefully harvested using a stereo-dissection microscope with which most of the soft tissue was removed without damaging the delicate bony structures. For multiple 3D imaging by neutron and laboratory X-ray tomography methods, 3 medaka and 4 zebrafish were maintained in water after dissection for reference-state imaging followed by immersion in deuterated water prior to and during additional tomographic imaging, as described below. Other medaka and zebrafish samples (n = 5 each) were dehydrated and prepared in different ways: one medaka and one zebrafish sample were fractured at the junction between the spines and the vertebral body and imaged by scanning electron microscopy; one medaka and one zebrafish sample were imaged by Zernike phase-contrast nano-CT; two medaka and two zebrafish samples embedded in polymethylmethacrylate were used in EDX and scanning electron microscopy; one medaka and one zebrafish sample were used in histological preparation and polarization light microscopy. Additionally, one vertebra of each fish species was analyzed by Raman spectroscopy. For all procedures described below, we analyzed the caudal part of the vertebral column of the fish. A schematic overview of the samples and the analysis performed is found in supplementary Fig. S1.

2.2. Neutron tomography

Prior to performing tomographies, the dissected vertebral columns of the three medaka and four zebrafish were maintained hydrated, immersed in water. Neutron imaging experiments were carried out at the CONRAD-2 neutron imaging beamline of the BER II reactor of the Helmholtz-Zentrum Berlin (HZB), Germany [59]. Measurements on the V7 experimental station were carried out 5 m downstream of the neutron guide, employing a high flux with an L/D of ~167. The samples were mounted onto a perforated Al grid, placed in a sealed aluminum chamber to minimize evaporation during measurement, and scanned by rotation in the imaging neutron beam (see additional supplementary methods information and supplementary Fig. S2). For each tomographic scan, 1250 radiographic projections were collected over an angular range of 360° with 1° increment and exposure times of 30 s per radiograph. Additional images of the empty beam (flatfield) and dark beam (dark field) were obtained for normalization. The imaging system used was a ZWO ASI1600MM Pro camera, 4656 × 3520 pixels with a pixel size of 3.8 μm focused on a neutron sensitive scintillator. To match the imaging system scintillator (10 μm thick), binning was employed to reach an effective pixel size of 7.6 μm. The sample to detector distance was set to 8 mm to maximize contrast. After imaging in the water saturation state, each sample was immersed in deuterated-water (D_2O) for at least 12 h (depending on scanner availability and recovery from experimental difficulties) and imaged again in the sealed aluminum chamber, fully saturated by deuterated-water.

The scans yield radiograms that contain information about the neutron attenuation due to scattering and absorption by the sample, and are extremely sensitive to changes in proton density (H^+) e.g. by removal of water. For quantification, conventional tomography reconstructions was performed including dark-field and flat-field corrections prior to reconstruction using the filtered back projection method of Octopus V8.5 (Zwijnaarde, Belgium). Multiple volume datasets were reconstructed per sample at different points in time. In total, fourteen datasets (medaka: n = 3 in H_2O, n = 3 in D_2O and zebrafish: n = 4 in H_2O, n = 4 in D_2O) were used for the analysis of changes in neutron attenuation due to water exchanged by D_2O in multiple vertebrae of medaka and zebrafish.

2.3. Laboratory based micro-computed X-ray tomography (μCT)

To help identify the water associated with the bone material, the same vertebral columns of the medaka and zebrafish samples that were previously scanned by neutron tomography were scanned with a desktop laboratory micro-computed tomography scanner (Skyscan 1172, Brucker-microCT Kontich, Belgium) (see setup in supplementary Fig. S3). Each sample was rehydrated with water, mounted in a PVA vial cushioned with moist foam to maintain humidity. All scans were performed with the X-ray source parameters set at 70 keV and 142 μA using a 0.5 mm aluminum filter and 4 μm effective pixel size. A total of 1200–1800 projections were acquired over an angular range of 360° for narrower and wider samples, respectively. Scans were reconstructed by the back projection algorithm using commercial software (NRecon 1.7.1.0 Bruker-microCT, Kontich, Belgium) and were examined in both

2D and 3D using Amira (AmiraZIBEdition version 2020.48, Zuse Institute Berlin (ZIB), Germany, and Thermo Fisher Scientific, Bordeaux, France) and ImageJ (ImageJ 1.52d, National Institutes of Health, USA).

2.4. 3D image registration

The reconstructed data acquired from neutron tomography and μCT were 3D registered by volume correlation in the Amira package, to enable quantitative assessment of regional scatter differences. 3D image processing made it possible to determine differences in the neutron signal due to water expelled from all the fishbone specimens. The difference in attenuation can be directly converted into estimates of water loss, because deuterated water has a very low neutron scatter cross-section and hence is not visible due to a low attenuation coefficient (μH_2O = 5.4 cm^{-1} vs μD_2O = 0.1 cm^{-1}). Datasets were visualized and cropped using ImageJ. For each vertebrae, we obtained 3D matched datasets corresponding to the sample originally immersed in water (H_2O-saturated dataset), the same sample after ~12 h of immersion in D_2O (D_2O-saturated dataset) and after scanning by μCT (labelled μCT dataset). The analysis procedure is illustrated in Fig. 1, depicting the digital registration process used to determine the amounts of water expelled from the bony regions of each vertebra. For each sample, datasets were loaded and displayed using the Amira Volren module. For co-registration, each water-saturated dataset was aligned with respect to the deuterium-saturated dataset (Fig. 1a, b), employing a mutual information correlation method. The attenuation difference between the aligned H_2O-saturated dataset and D_2O-saturated dataset of each sample corresponds to the loss of H^+ signal, due to water that was expelled from the volume inside the bone by ambient D_2O diffusion (Fig. 1c, expelled H_2O dataset). In a subsequent step, reconstructed X-ray tomography datasets of the same bones were used to identify the mineralized regions of the vertebra to separate bony from non-bony domains. These data were used to mask the neutron data ensuring isolation of regions corresponding to water loss in bone only (excluding soft tissue). The μCT datasets were segmented using the AMIRA segmentation editor and three caudal vertebrae were selected in each skeleton, as indicated by the region marked by the blue-outline in Fig. 1c. The resulting binary volume (labeled μCT dataset) was aligned and co-registered with respect to the expelled water volume (expelled H_2O dataset) and used to precisely map the neutron signal from expelled water to within < 10 μm uncertainty in the bony region of each vertebra in each sample (Fig. 1d). The obtained water expelled data was analyzed as described in following sections.

2.5. Water content analysis

Obtained volumes of neutron attenuation difference, corresponding to the water expelled exclusively from bone, were compared with the water-saturated data, making it possible to determine % differences in the amount of water expelled. Both the absolute amount of expelled water and the % difference were used for further analysis along the vertebral column axis on a slice by slice (7.6 μm thick) basis. To test for uncertainty in the co-registration of the X-ray and neutron data, ensuring that only bony regions were included in the analysis, ImageJ was used to erode the vertebra μCT masks by one layer of pixels, effectively making the

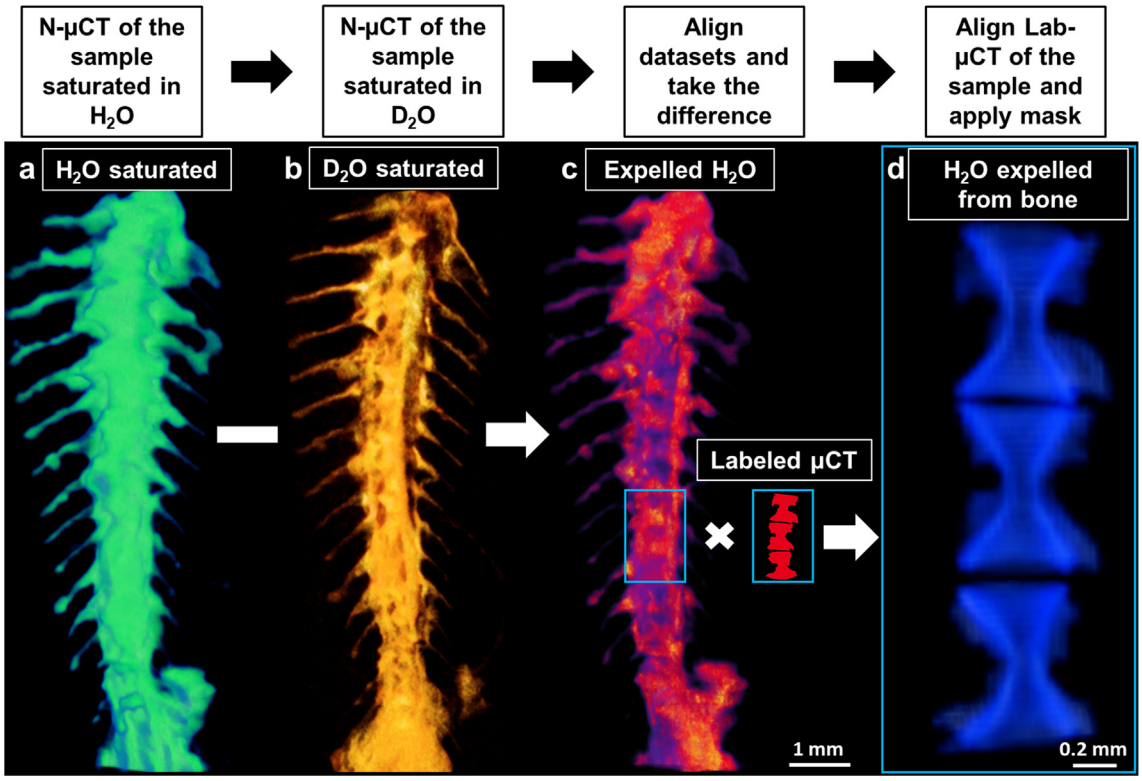

Fig. 1. Overview of 3D water quantification procedures and the accompanying image analysis workflow from left to right: (a) 3D-rendering view (green tones) of an example of a neutron tomography (N-μCT) of a water (H_2O) saturated dataset, depicting the caudal segments of the vertebral column of one fish. (b) 3D-rendering view (orange tones) of an N-μCT of a sample in deuterated water (D_2O), observed for the same caudal region shown in (a). Alignment of H_2O and D_2O datasets by 3D registration to calculate the differences in the signal. (c) a 3D-rendering of water volume expelled, based on the difference between the registered D_2O saturated and H_2O saturated datasets. (d) The bone region of interest of the caudal vertebrae (marked by the blue rectangle) was masked for quantitative analysis of the expelled water by matching the neutron tomography with X-ray μCT scans of the vertebral bones. (For interpretation of the references to color in this figure legend, the reader is referred to the web version of this article.)

bones smaller by removal of voxels on all bone-air interfaces. This made it possible to compare water-loss results between the masked data and eroded medaka and zebrafish geometries to remove possible partial volume effects. For statistical analysis, comparable sized segments of the Caudal cone (CdC), Centrum middle (CM), and Cranial cone (CrC) regions of each vertebra were evaluated. Quantification was based on sixteen cross-sectional slices from each of the CM, CrC, and CdC regions of each vertebra, in which the average neutron intensity difference (H_2O minus D_2O) was analyzed.

2.6. Zernike X-ray phase-contrast nanotomography

The spines of one medaka and one zebrafish vertebrae were imaged at the nanotomography endstation of the P05 imaging beamline at PETRA III, DESY, Hamburg, Germany, operated by Helmholtz-Zentrum Hereon. A detailed description of the setup is provided elsewhere [60]. The < 100 μm thick spines are well suited for imaging in the extremely restricted nanobeam field of view. Each sample was mounted on top of a pin holder, and regions of interest were imaged using a large field of view (∼ 80 μm) in the transmission X-ray microscope (TXM) using Zernike phase-contrast enhancement. Nanotomography was performed with 1529 angular steps covering 180° rotation range with 559 ms exposure times. Projections were acquired at 11 keV with an effective pixel size of 35.9 nm.

All tomographic scans were normalized by flat-field projections acquired at the beginning and the end of each scan. The tomographic reconstructions were performed using the Gridrec algorithm [87] and a Shepp Logan filter in the TomoPy package [88]. The datasets were imported to ImageJ to visualize the ultrastructure of both bone types.

2.7. Scanning electron microscope

For scanning electron microscopy (SEM), three medaka and three zebrafish samples were dehydrated in ascending graded series of ethanol solutions (50 %, 75 %, and 100 %). For each species, one of the spines was fractured to expose transverse surfaces. Samples were gold coated and imaged in a Phenom-XL G2 scanning electron microscope (Thermofisher, Eindhoven, The Netherlands) with the backscatter imaging mode at 5 keV acceleration voltage using the high vacuum 0.1 Pa imaging mode. The other samples were embedded in polymethylmethacrylate and analyzed in Cam-Scan MaXim SEM under low vacuum equipped with a Bruker 6 XFlash 6130 EDX energy dispersive X-ray spectrometer. One additional sample of each species was scanned in the Phenom-XL in backscatter mode.

2.8. Histological staining

The caudal vertebrae of medaka and zebrafish specimens were fixed in 4 % buffered paraformaldehyde for 48 h at 4 °C. After fixation, the specimens were decalcified by immersion in 0.5 M ethylenediaminetetraacetic acid (EDTA) solution for three days (pH 7.4). Thereafter the specimens were dehydrated in ascending concentrations of ethanol (70 %, 80 %, 96 %, and 100 %), cleared with xylene, and embedded in paraffin. The bones were then cut into 2 – 4 μm thick histological sections using a diamond microtome and were mounted onto glass slides. After deparaffinization and rehydration, the tissue sections were stained with Alcian blue (Alcian blue 8GX solution, pH 2.5, Sigma Aldrich; 05500) following standard protocols [61]. Nuclear fast red-aluminum sulfate (Chroma Waldeck, Germany) was used as counterstaining. The stained tissue sections were examined at a × 50 magnification using a digital multi-focus stereo microscope (Keyence DigitalmikroskopVHX – 500, Keyence Corporation; Neu-Isenburg, Germany). Strongly acidic mucosubstances (proteoglycans) in the bone were identified based on color.

2.9. Quantitative polarized microscopy

Histological bone sections were imaged in a Leitz transmission microscope with a × 25 lens, using an Optoviz Imaging polarization image system comprising an Optoviz Polarization Control Unit and PixeLINK camera (PLD752CU, 5.86 × 5.86 μm pixel size) mounted with a 632 nm bandpass filter. The automated polarizers make it possible to quantify orientation and retardance of the light due to interactions with the anisotropic collagen fibers, useful for identification of fiber orientation in both medaka and zebrafish [47]. The polarization orientations of fibers in the histological sections were determined using the Optoviz Analysis software.

2.10. Raman spectroscopy

Raman microspectroscopy was used to analyze three different regions of one medaka and one zebrafish sample. Measurements were conducted by means of a WITec alpha 300R confocal Raman micro-spectrometer (WITec, Ulm, Germany) equipped with a frequency-doubled Nd:YAG laser operating at 532.15 nm. The instrument has a 300 mm focal length spectrograph with a 600 lines/mm grating, yielding a spectral resolution of approximately 4 cm^{-1}. Rayleigh scattered light was blocked by an edge filter while Raman backscattered radiation was coupled into a 100 μm multimode fiber guiding the light onto an electron multiplying charge-coupled device (EMCCD) camera with 1600 × 200 pixels (Andor, DU970N-BV-353, Andor Technology Plc, Belfast, Ireland). A Nikon CFI S Plan Fluor ELWD 40x objective with a numerical aperture of 0.6 and a working distance of 2.80 – 3.60 mm focused the laser light onto the samples. Raman spectra were recorded in the spectral range between 400 and 3800 cm^{-1}. Acquisition times of individual spectra were 30 s. The laser power at the sample plane was approximately 10 mW. For data acquisition and spectra analysis (removal of cosmic rays, fluorescence baseline correction, cutting, normalization, averaging) WiTEC's Project Five (v. 5.1) software package was used.

2.11. Statistical analysis

Statistical analyses were performed using RStudio (RStudio Version 1.3, RStudio, PBC, Boston, MA). To compare the amount of expelled water along medaka and zebrafish bone in the CM region and in combined CrC and CdC regions before and after digital erosion the nonparametric Wilcoxon rank-sum test was used. The Wilcoxon signed-rank test was applied to compare the percentage of expelled water between the CM region and the combined CrC and CdC regions, before and after digital erosion of both medaka and zebrafish. P-values < 0.05 were considered statistically significant. Correlation of the attenuation before and after 3D erosion of the CM region and the combined CrC and CdC regions of both medaka and zebrafish was performed by regression analysis, for which confidence intervals are reported.

3. Results

The X-ray μCT revealed all the main details in both zebrafish and medaka, with geometries similar to those previously described by Ofer et al. [49,47] and Suniaga et al. [62]. Fig. 2 presents the typical morphology of the caudal vertebra of medaka and zebrafish as shown by μCT. The amphicoelous bone centrum in both (Fig. 2. a1, b1) comprises three distinct zones: The near-cylindrical central

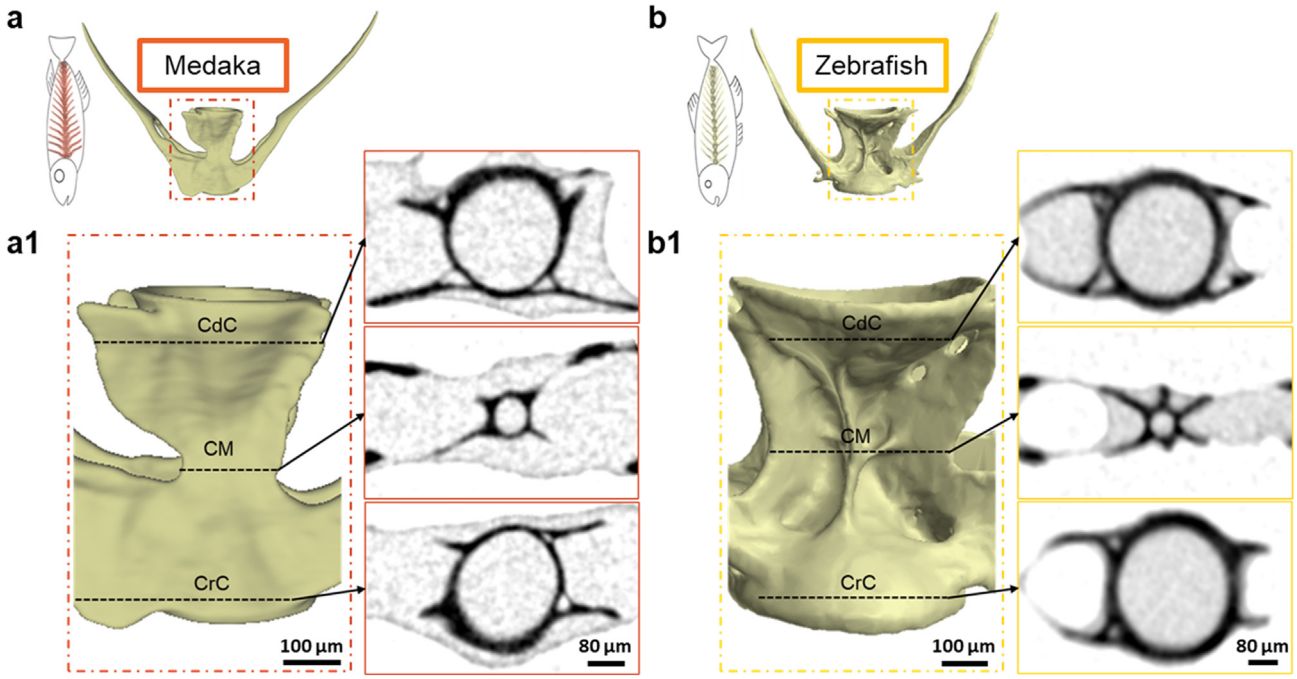

Fig. 2. Overviews of (a) medaka and (b) zebrafish vertebra bones: 3D reconstructed low resolution lab µCT results. The dash-dotted insets identifies the amphicoelous centrum region of (a1) medaka and (b1) zebrafish vertebrae. Three virtual cross-sectional slices in the 3D data (dashed lines) of medaka and zebrafish are shown in detail, exposing the different regions of the centrum: Caudal cone (CdC); Centrum middle (CM) and Cranial cone (CrC).

zone of the centrum (CM) and the cranial and caudal cone-shaped regions of the centrum (CrC and CdC, respectively). Both CrC and CdC cones show a similar symmetric shape with thin walls ~ 20 µm thick, where the diameters of the cones increase towards the outer ends as compared with CM region. This region exhibits a narrow cylindrical shape with lateral axial bars (septa) acting as supports. The CM regions of medaka and zebrafish differ slightly with zebrafish exhibiting more prominent lateral septa. Supplementary information videos S1 and S2 showcase typical vertebra structures in medaka and zebrafish, respectively. These features are also observed in backscatter SEM images of longitudinal slices in typical medaka and zebrafish vertebra (Fig. S4 of the supplementary Information), demonstrating the overall geometrical similarities between the two species. EDX analysis (supplementary Fig. S5) shows similar elemental composition of calcium, phosphorous and oxygen except for carbon which is slightly higher in zebrafish bone as compared to medaka bone.

SEM images of fracture surfaces of medaka (Fig. 3a) and zebrafish bone (Fig. 3b) reveal hints to the present of mineralized collagen fibers. These are the fundamental building blocks of all bone biocomposites. In the more structurally homogenous medaka, it is easier to observe large regions of textured layered collagen bundles (Fig. 3a) with the fracture surface inducing occasional pullout of the collagen fibers (red arrows). In the zebrafish sample, the fracture surface exposes osteocyte lacunae (yellow asterisks) within the bone matrix (Fig. 3b). Also in this bone, ripped-out collagen fibers are occasionally visible on the exposed surfaces between lacunae. The nanostructure of the bone of both species is further revealed by Zernike phase-contrast nano-CT. The difference in void distribution is clearly exhibited due to the enhanced edge contrast and nanometer resolution. As shown by a longitudinal section (Fig. 3c), intricate details of the textured nanofibers are disclosed in the medaka compact bone where layers with variable degrees of contrast are visible. The lack of any trace of LCN porosity is typical for this bone and stands in contrast to what is identified in a longitudinal section of zebrafish bone that highlights the presence of voids (fFig. 3d). Both osteocyte lacunae as well as smaller voids of sections through canaliculi channels are seen. The voids in zebrafish bone are further illustrated in 3D in supplementary Fig. S6, showing a 3D rendering of this data for a spine section of zebrafish bone. The contrast-enhanced volume images generated with Zernike phase-contrast nano-CT prove that the images obtained by SEM (Fig. 3a, b) are typical for the full volume of these bones. Note however, that due to phase-contrast enhancement, mineral density cannot be extracted from the Zernike nano-CT data. Supplementary information videos S3 and S4 showcase medaka and zebrafish bone ultrastructures, respectively.

The neutron tomography volumetric attenuation values from each of the 21 vertebrae analyzed were converted into estimates of the amount of water expelled. Example renderings of the 3D difference data are given in Fig. 4 in which (a) medaka bones are seen to lose far more water as compared with (b) zebrafish bone. The figure demonstrates the quantitative spatial data available for each specific anatomical region in each of the analyzed vertebrae. The CM and CdC and CrC regions are marked for clarity. The red shades in Fig. 4 correspond to regions where higher percentages of expelled water were observed. Analysis of the spatial distribution of this data formed the basis for evaluation of all bone regions.

Quantitative statistical evaluation of the different vertebra regions highlights the significantly higher amounts of expelled water observed in the anosteocytic medaka bone, as compared with osteocytic zebrafish bone (Fig. 5). The average amount of expelled water for all medaka and zebrafish bones in the CM region and the combined CrC and CdC regions, as well as comparisons of the percentage of average expelled water between medaka and zebrafish in the CM region and the combined CrC and CdC regions before and after morphological erosion are presented in boxplots (Fig. 5). The plots show the minimum, median and maximum values, as well as 25*th* and 75*th* percentiles for each fish species. Table 1 provides details related to the information used to construct the boxplots of Fig. 5. The results show that there is a significant difference ($p < 0.05$) between species, where medaka loses

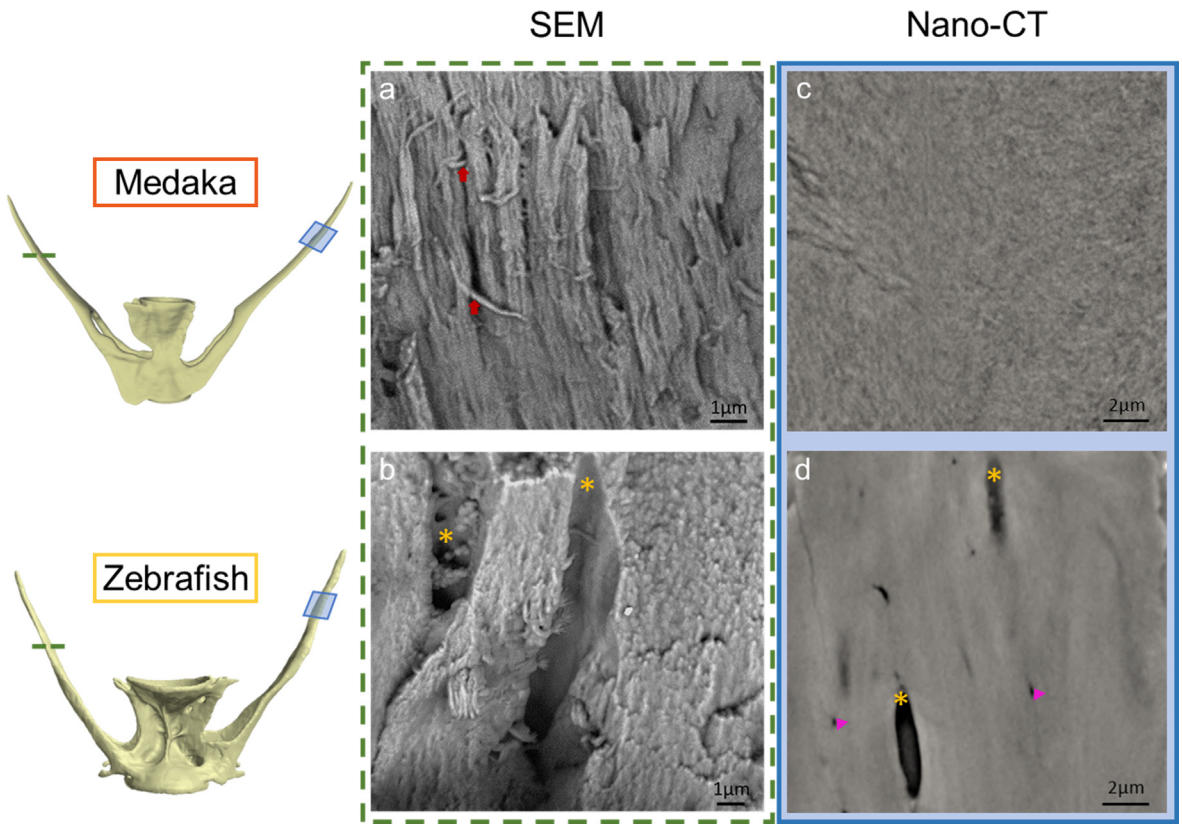

Fig. 3. Comparable fibril ultrastructure of (a, c) medaka and (b, d) zebrafish bone. SEM images (a, b) of fracture surfaces expose ripped-out collagen fibers. (a) The fracture surface within medaka bone exposes arrays of parallel-laying collagen bundles. In some regions, collagen fiber pullout is seen (red arrows). (b) In zebrafish, osteocytic lacunae (yellow asterisks) are observed within layers of mineralized collagen fibers revealing exposed fibers with occasional pullout. The SEM images can be compared to slices obtained in intact samples imaged by Zernike phase contrast nano-CT. Longitudinal sections (c) show the compact bone structure of medaka bone, revealing bundles of collagen fibers with different contrasts. In the longitudinal section of zebrafish bone (d), the osteocytic lacunae appear as prominent elongated voids (yellow asterisks) and canaliculi are seen as smaller voids (pink triangles). (For interpretation of the references to color in this figure legend, the reader is referred to the web version of this article.)

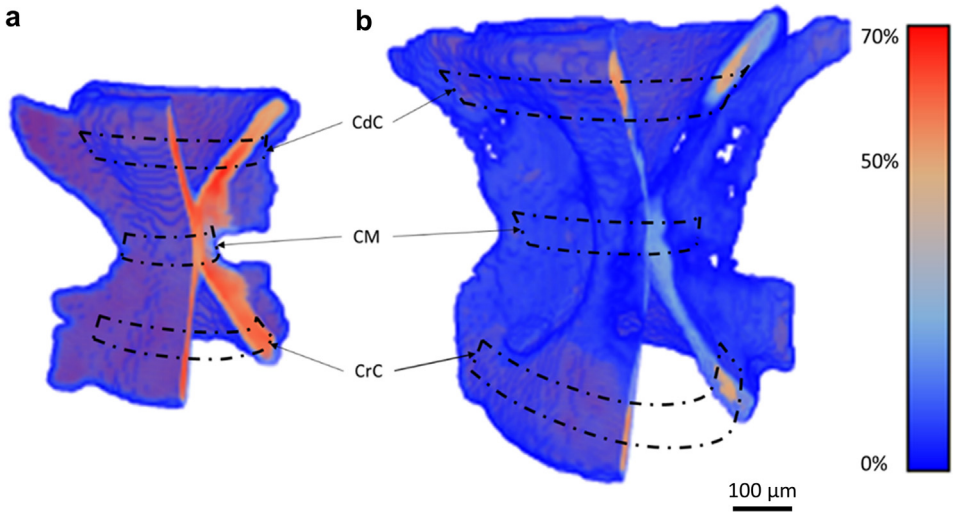

Fig. 4. 3D-rendering of variations in water that was expelled from (a) medaka and (b) zebrafish vertebrae. Though somewhat different in macroscopic size, the similar-thickness bones disclose that a much higher percentage of water was removed from medaka bone than from zebrafish bone. In blue regions, less water was expelled, and in red regions, more water was expelled. Dash-dotted rectangles identify the Cranial cone (CrC), Centrum middle (CM), and Caudal cone (CdC) regions used for quantitative analysis of the expelled water for both medaka and zebrafish bone. (For interpretation of the references to color in this figure legend, the reader is referred to the web version of this article.)

almost 25 % more water as compared with zebrafish. No significant difference ($p > 0.05$) was found between the CrC and CdC regions and CM region of each fishbone. Intra sample comparisons of the entire original versus eroded bone geometries in each sample show a trend but did not reach significant statistical difference ($p > 0.05$). Nevertheless, slicewise comparisons of each slice with itself before and after erosion (supplementary Fig. S7) suggest that in medaka, results of expelled water measured by neutron tomography and

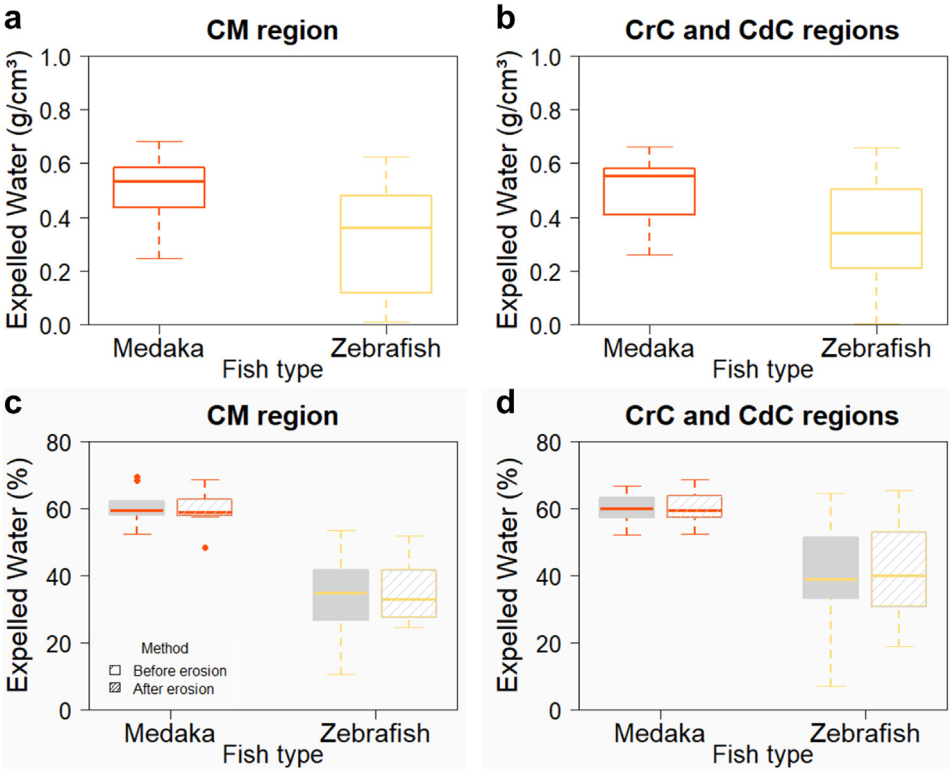

Fig. 5. Comparison of the average amounts of expelled water (g/cm^3) determined in each bone region, observed for 2D slice-by-slice analysis of the medaka and zebrafish 3D data. A direct comparisons of (a) CM region and (b) the combined CrC and CdC regions reveals differences in the amount of expelled water between medaka and zebrafish. When divided by the measurements obtained for fully hydrated bones (H_2O datasets), substantital differences in the relative amounts of water expelled become evident for (c) the CM region and (d) the combined CrC and CdC regions. Comparisons are also made with eroded datasets, corresponding to reduced-sized, inner bony regions, and provided here to rule out partial volume effects in which the accidental inclusion of soft hydrated tissue may contribute on non-mineralized surfaces of the bones.

Table 1
Percentage of expelled water at a) the CM region and b) the CrC and CdC regions.

a) Percentage of expelled water in the CM region*	Medaka (n = 9 vertebra)		Zebrafish (n = 12 vertebra)	
	Before erosion	After erosion	Before erosion	After erosion
Median (%)	59.42	58.80	34.81	32.94
Mean (%)	60.76	60.11	34.44	35.54
Stdev	5.32	6.15	11.95	9.78
IQR	4.06	4.78	13.50	13.39
25*th* Percentile	58.00	57.83	27.76	27.69
75*th* Percentile	62.06	62.61	41.26	41.07
Min	52.37	48.31	10.52	24.57
Max	69.40	68.64	53.57	51.99
b) Percentage of expelled water in the CrC and CdC regions**	Medaka (n=9 vertebra)		Zebrafish (n=12 vertebra)	
	Before erosion	After erosion	Before erosion	After erosion
Median (%)	60.03	59.50	38.83	40.09
Mean (%)	60.10	60.11	40.60	41.41
Stdev	4.06	4.17	13.29	13.25
IQR	5.55	5.94	18.10	21.34
25*th* Percentile	57.53	57.64	33.35	31.21
75*th* Percentile	63.08	63.58	51.44	52.55
Min	52.09	52.55	7.05	19.04
Max	66.88	68.57	64.56	65.49

* n = 16 slices per vertebra.
** n = 32 slices per vertebra.
Wilcoxon tests show a significant difference ($p < 0.05$) between species yet no significant difference ($p > 0.05$) between the CrC and CdC regions and CM region nor between the entire original bone and eroded bone of each sample.

masked by X-ray tomography are not affected by the presence of voids and soft tissue. Yet for zebrafish, there appears to be a noticeable partial-volume effect, as slicewise correlation identified 30 % less water loss in eroded bones, as compared with the complete bones, not clearly visible in the average results presented in Fig. 5. Cumulative water-loss mean and standard deviation results

for each vertebra of each sample before and after erosion are listed in Supplementary Tables S1 and S2. These results show that much more water diffuses across the ECM in medaka than in zebrafish bone.

To find possible explanations for our 3D data, further analysis was performed by Raman spectroscopy, histological staining and automated polarization analysis. Reminiscient of the EDX data (supplementary Fig. S5), Raman microscopy (Fig. 6a, b) revealed that both bone species have similar compositions except that this method reveals a strong difference in the 1375 cm^{-1} vibration band, which is hardly visible in medaka bone. Raman spectra of both bones show characteristic bands of mineral at 961 cm^{-1} (ν_1, phosphate) and 1070 cm^{-1} (ν_1, carbonate) as well as organic content, for example at 1445 cm^{-1} ($\delta(CH_2)$ of proteins) and 1669 cm^{-1} (amide I band of proteins), but medaka does not include the 1375 cm^{-1} band, which has been previously associated with PGs in mammalian bone [63,64]. Medaka and zebrafish bone histological sections stained with Alcian blue (Fig. 6c, e) indicate considerable differences in the present of GAGs [65–67]. In medaka bone (Fig. 6c), there is little blue stain to be seen. Zebrafish (Fig. 6e) however is strongly stained due to positive reactions with the Alcian blue dye. The outer and inner sides of both bone sections are counterstained in pink due to soft tissue reaction with nuclear fast red-aluminium sulfate which stains nuclei and cytoplasm. The same samples imaged by quantitative polarization microscopy revealed no difference in the orientation of collagen fibers in medaka (Fig. 6d) and zebrafish (Fig. 6f) bone. In both species, a layered highly ordered structure of collagen appears to reside in concentric layers around the cones as shown previously, where the bright regions reveled by polarized orientation analysis are mainly aligned parallel to each other.

4. Discussion

This study revealed that large amounts of water are free to diffuse out of anosteocytic medaka bone under ambient conditions, whereas water is largely retained within the osteocytic zebrafish bone matrix. These findings suggest that water has different mobility in the ECM of the two bone matrix types, independent of the presence of osteocyte lacunae. This is a surprising outcome because very little free water is expected to come out of the LCN-free medaka bone matrix, or, at the very least, the two bone materials should exhibit similar permeability. It is widely assumed that water freely flows through the micrometer and nanometer porosities of the LCN system (sized several μm down to ~100 nm) [44]. However, results show that water in the zebrafish bone matrix surrounding the LCN is far less mobile as compared with the ECM of medaka. These findings are even more unexpected because the bones of both fish species present similar mineralized collagen fiber morphology. The only plausible explanation for this difference is that the bone matrices of the two species differ by some fundamental ingredient of the composite, which affects their water permeability. Histological and Raman results identify this ingredient to be PGs.

The reduced H^+ scattering observed (~ 60 vol%) in both the CM region and the CrC and CdC regions of medaka bone arises from water that resides within the bone ECM because these bones are poorly vascularized and lack LCN porosity (see Fig. 3c, d). Yet in the bones of zebrafish, only ~33 % to ~39 % of the signal decreased following long immersion in D_2O. Assuming that similar to mammalian bone, water comprises approximately 20 % of zebrafish bone [17], we can therefore estimate that < 7 % of the volume of water was exchanged in our experiments. This volume roughly

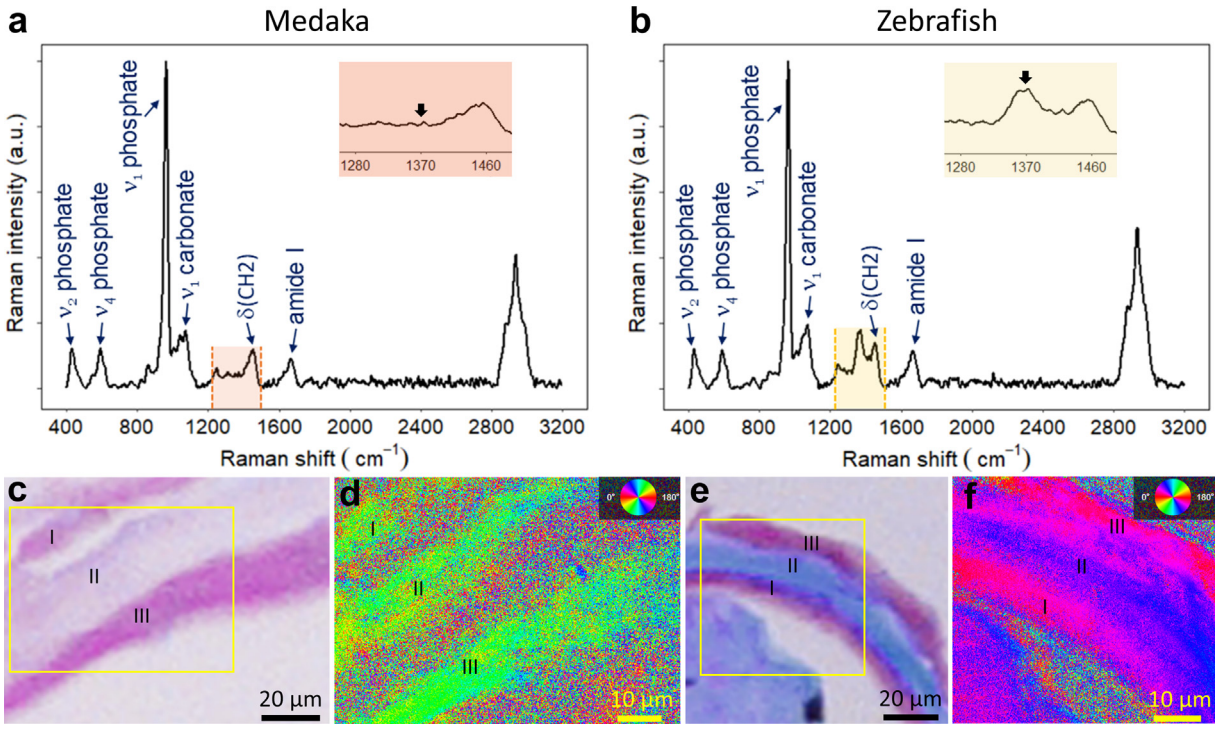

Fig. 6. Average Raman spectra from different analyzed points in the vertebra bone of (a) medaka and (b) zebrafish. Raman spectra shown is an average of multiple baseline corrected and normalized spectra. Black arrows indicate the 1375cm^{-1} band associated with PGs, highlighting the difference observed in the mineralized samples. Images of Alcian blue histological staining of demineralized (c) medaka and (e) zebrafish bone show strong blue stain in zebrafish bone compared to medaka bone. The connective tissues surrounding bone sections is counterstained in pink. Quantitative polarization analysis of collagen orientation maps of the same histological samples of medaka (d) and zebrafish (f). Collagen fiber layers marked I, II, III in both bone sections are detected by polarized light, mainly oriented parallel to each other along the outer rims of the CrC and CdC cones. (For interpretation of the references to color in this figure legend, the reader is referred to the web version of this article.)

corresponds to the volume of water residing in the LCN and in the nano porosity, according to the following calculation: From previously published data, we calculated that about ~1.1 % of zebrafish bone consists of lacunar porosity (see supplementary Fig. S8). Based on literature reports it can be concluded that canalicular porosity adds twice this value [68–70] and additional nano porosity reportedly accounts for ~4 % of the total volume [10]. Therefore, assuming the micro and nanoporosity is open, it is possible that the signal detected by neutron tomography in zebrafish arises mostly from water exchange in the pores. This suggests that in osteocytic bone, the ECM and LCN compartments are separate, such that water inside the bone porosity is mainly confined to move along pressure gradients within the LCN but not across the ECM matrix.

Medaka bone results suggest that water can diffuse and easily exchange within the ECM. Therefore, the nano-scale porosity (at the mineralized fiber collagen-apatite length scale) of anosteocytic bone is open and connected. It has been shown that medaka bones have a slightly higher mineral density than zebrafish, which rules out the possibility of larger pores in the medaka mineralized matrix [47]. SEM and Zernike phase-contrast nano-CT images of medaka bone reveal no trace of larger pores within bone matrix. Intriguingly, EDX analysis in zebrafish disclose a slightly higher carbon content than medaka bone (Supplementary Fig. S5) but EDX showed similar Ca, O and P content in both bones. Raman spectroscopy, correlated with histological staining, identified the 1375 cm^{-1} band associated with PGs to be present in zebrafish but almost absent in medaka bone. In mammalian bone, this vibration band has been reported to arise from PGs, specifically GAG side chains, and it is used as a PGs marker in both cartilage and bone [63,64,71]. GAG chains attached to core PG proteins attract water inside the bone matrix since they are highly polar [12,14]. All of the above raises the possibility that the bony matrix of osteocytic bone may be relatively impermeable to water, due to the presence of water-confining PGs, effectively isolating the ECM from the free water in the relatively large LCN pores [72]. We therefore propose that PGs may modulate the extent of water binding within the ECM.

Several published works proposed poroelasticity theories of transduction in osteocytic bone. According to such models, fluid flow through the osteocyte canalicular network of pores plays a crucial role in the biologic response of bones to load, being the most likely mechanism for mechanotransduction [9,35,36,73]. Cowin *et al.* proposed that when bone experiences mechanical loading, the fluid is pressurized around osteocytes before the fluid is driven to flow [35,40]. For such a mechanism to operate, the ECM matrix surrounding the internal open porosity must be relatively impermeable [40]. Previous work has estimated permeability based on theoretical analysis, reporting a range of 10^{-17} to 10^{-20} m^2 in mammalian bone. Experimental verification studies reported permeability values to range from 10^{-22} to 10^{-25} m^2 [74,75]. Our neutron data observations of restricted water flow in osteocytic (zebrafish) bone are in line with these observations by others.

The findings of the present study suggest that PGs may be modulators of how water may be retained within the lacuna-canalicular open network of pores. Several works have reported that the pericellular matrix surrounding the osteocytes within the lacunae and canaliculi also contains PGs, glycoproteins, and hyaluronic acids that form a tether mesh, glycocalyx, that attaches the osteocyte membranes to the surrounding bone-matrix walls [76–80]. The glycocalyces may amplify the sensation of load by osteocytes through shear drag forces in response to fluid flow [41,81]. Though the mechanism by which bone cells sense mechanical stimuli is currently not fully understood, evidence suggests that fluid flow plays an important sensory role, therefore confinement of water flow to the LCN may be crucial for bone function.

The expelled water analysis was based on the examination of average values in a 2D slice-by-slice analysis along the axial vertebral orientation. Indeed, SEM and CT images show bone in the CrC and CdC regions to be thicker than at the CM region, no significant differences was found in the amount of water expelled between the regions of both species ($p > 0.05$). This rules out any role that bone thickness may have on the results. Boxplots (Fig. 5) show much higher variance in the expelled water results for zebrafish, which can be attributed to the heterogeneity of the internal LCN porosity within these bones. It is likely that the amount of expelled water in some of the zebrafish regions is affected by partial volume effects associated with the presence of osteocytes because, following the morphological erosion of these datasets, most slices exhibited 30 % less water loss prior to erosion (Supplementary Fig. S7). Furthermore, the variance in the amount of expelled water between slices in the vertebrae of the zebrafish samples before and after erosion is much higher than between slices in medaka bone. Though erosion did not significantly change the results shown in Fig. 5, they add corroborating evidence to the general observation that more water diffuses across medaka bone as compared to zebrafish bone material.

Though neutron tomography is limited in resolution, it is extremely sensitive and consequently it was possible to evaluate in 3D the amount of water expelled from the bone matrix of the sub-mm sized samples. Neutron tomography was previously used to investigate the bone-implant interface due to its capability to decrease artifacts arising from metallic structures [82,83,58]. In combination with modest resolution (>4 μm) X-ray μCT, neutron tomography provided insights into the diffusion and distribution of the water within the bone ECM. Jointly, these methods made it possible to mask and exclude water signals from soft tissues located on the outer srfaces of the bones, as ensured by morphologic erosion (Supplementary Fig. S7). The higher resolution Zernike phase-contrast nano-CT directly reveals in 3D the main LCN porosity difference between the two fishbone ultrastructures. In this respect, the present findings match well observations by other authors who used atomic resolution NMR, but where only a small fraction of the bone was analyzed [17,84,85,86]. There are multiple reports of NMR water exchange studies, where the water was gradually replaced by deuterated water until equilibrium was reached. One report found that even at equilibrium, 30 % of the initial water content still remained in the bone [17]. Complete removal of water from bone is likely only possible upon thermal activation and sample heating to reach evaporation at 100 °C. In our study, samples were exchanged in deuterium for 12 h under ambient conditions, which may not be enough time to fully exchange all the water within the bone samples. Though some authors claim that sufficient heavy water equilibrium is reached already within 8 h [84] others propose longer immersion times [82]. Nonetheless, the results shown here clearly reveal significant differences in water diffusion across the two bone material that we analyzed and future studies may quantify diffusion dynamics in additional bone types.

Based on the findings in the present study, we propose that the bone ECM contains a mechanism to modulate the permeability to water and that PGs are the most likely candidate regulators of this permeability. Our proposal is outlined schematically in Fig. 7. Though the bone material of anosteoctytic fish (Fig. 7a) lacks open porosity associated with osteocytes, its nanocomposite structure allows for significantly more diffusion of water. This may be an evolutionary alternative to the lacuna-canalicular system, which raises the possibility that the two bone materials might have different mechanosensation mechanisms. A water-tight bone matrix surrounding the LCN ensures that deformation due to mechanical loading leads to fluid flow around cells in the LCN. In this manner, load may be transmitted to the osteocytes according to hydraulic

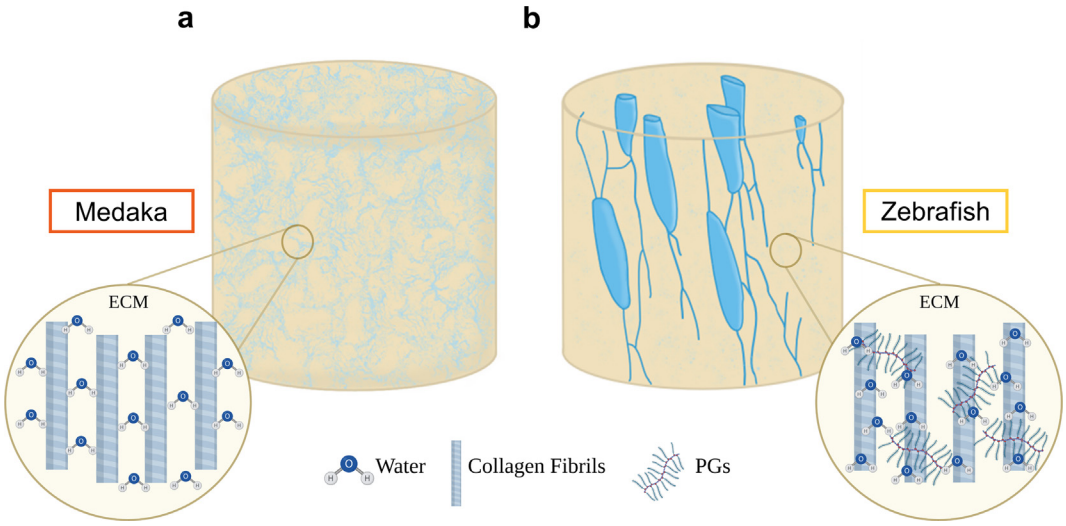

Fig. 7. Schematic representation of our proposed model for water permeability in the ECM of anosteocytic versus osteocytic bone. Water (colorized blue) within bone matrix of (a) anosteocytic fishbone is loosely bound to the organic component of the ECM. (b) In osteocytic fishbone, water mainly flows through the lacuna-canalicular porosity, and there is little or no diffusion of water across the bone matrix ECM since PGs retain the water. The schematic illustration is not drawn to scale. (For interpretation of the references to color in this figure legend, the reader is referred to the web version of this article.)

pressure gradients. We propose that reasonably watertight bone material in the ECM is essential for a poroelastic-active mechanosensory response of osteocytic bone (Fig. 7b) to operate [78]. If indeed this is the case, it may be extended to explain aging or pathological changes in bone mechanobiology that may be related to alterations in the distribution of PGs and water [13]. In other words, PGs may affect how permeable bones become, and they may therefore change over time. Further studies are needed to better characterize how and why certain bones or bone regions may alter water diffusion across the ECM.

5. Conclusion

Our work using neutron tomography revealed that water is freer to diffuse out of anosteocytic medaka bone, as compared with osteocytic zebrafish bones. About ~60 % of water was expelled from medaka bones contrasting the 33 % ~ 39 % water that is expelled from the bones of zebrafish. This raises the possibility that the bone matrices of the two species is fundamentally different, not just due to the presence or absence of osteocytes in the bone. These results are based on combining X-ray and neutron contrasts, merged and quantified by 3D image correlation that is completely observer-independent. PGs distributions are likely different between the ECM of medaka and zebrafish bone, which suggests that they may modulate how permeable the ECM is to water. PGs in the matrix may therefore tune the leakiness and hence the sensitivity of the LCN to poroelastic mechanotransduction in osteocytic bone.

6. Date availability

The raw and processed data required to reproduce these results are available upon reasonable request by contacting the authors.

Data availability

Data will be made available on request.

Declaration of Competing Interest

The authors declare that they have no known competing financial interests or personal relationships that could have appeared to influence the work reported in this paper.

Acknowledgements

A. S., P. Z. and R. S. gratefully acknowledge the financial support from the German Research Foundation (DFG) grant ZA557/5. E. L. and I. G. gratefully acknowledge the financial support from the DFG-SFB 986, project Z2.

We thank the Helmholtz-Zentrum Berlin für Materialien und Energie for the allocation of neutron beamtime on BER II. We acknowledge DESY (Hamburg, Germany), a member of the Helmholtz Association HGF, for the provision of access to synchrotron radiation. Parts of this research were carried out at PETRA III beamline P05.

We thank Dr. Daniel Baum and Zuse Institute Berlin for providing access to Amira ZIB-Edition and we thank Marion von Zitzewitz for help in preparing the histological stain sections.

Parts of Fig. 7 and supplementary Fig. S1 and S3 were created with the BioRender.com platform.

Appendix A. Supplementary material

Supplementary data to this article can be found online at https://doi.org/10.1016/j.matdes.2022.111275.

References

[1] S. Weiner, H.D. Wagner, The material bone: structure-mechanical function relations, Annu. Rev. Mater. Sci. 28 (1998) 271–298, https://doi.org/10.1146/annurev.matsci.28.1.271.

[2] J.-Y. Rho, L. Kuhn-Spearing, P. Zioupos, Mechanical properties and the hierarchical structure of bone, Med. Eng. Phys. 20 (1998) 92–102, https://doi.org/10.1016/S1350-4533(98)00007-1.

[3] J. Currey, Hierarchies in biomineral structures, Science 309 (2005) 253–254, https://doi.org/10.1126/SCIENCE.1113954.

[4] S.R. Stock, The mineral-collagen interface in bone, Calcif. Tissue Int. 97 (2015) 262–280, https://doi.org/10.1007/s00223-015-9984-6.

[5] A.L. Boskey, Noncollagenous matrix proteins and their role in mineralization, Bone Mineral 6 (1989) 111–123, https://doi.org/10.1016/01696009(89)90044-5.
[6] R.A. Robinson, S.R. Elliott, The water content of bone. I. The mass of water, inorganic crystals, organic matrix, and CO2 space components in a unit volume of the dog bone, J. Bone Joint Surgery Am. 39 (1) (1957) 167–188.
[7] K.H. Mueller, A. Trias, R.D. Ray, Bone density and compositon. Age-related and pathological changes in water and mineral content, J. Bone Joint Surgery Am. 48 (1966) 140–148.
[8] C. Frantz, K.M. Stewart, V.M. Weaver, The extracellular matrix at a glance, J. Cell Sci. 123 (2010) 4195–4200, https://doi.org/10.1242/jcs.023820.
[9] S.C. Cowin, G. Gailani, M. Benalla, Hierarchical poroelasticity: movement of interstitial fluid between porosity levels in bones, Philos. Trans. Ser. A, Mathematical Phys. Eng. Sci. 367 (2009) 3401–3444, https://doi.org/10.1098/rsta.2009.0099.
[10] T. Tang, W. Landis, E. Raguin, P. Werner, L. Bertinetti, M. Dean, W. Wagermaier, P. Fratzl, A 3D network of nanochannels for possible ion and molecule transit in mineralizing bone and cartilage, Adv. NanoBiomed. Res. (2022) 2100162, https://doi.org/10.1002/anbr.202100162.
[11] J.D. Currey, Bones: Structure and Mechanics, Princeton University Press, 2002.
[12] R. Hua, Q. Ni, T.D. Eliason, Y. Han, S. Gu, D.P. Nicolella, X. Wang, J.X. Jiang, Biglycan and chondroitin sulfate play pivotal roles in bone toughness via retaining bound water in bone mineral matrix, Matrix Biol. 94 (2020) 95–109, https://doi.org/10.1016/j.matbio.2020.09.002.
[13] X. Wang, R. Hua, A. Ahsan, Q. Ni, Y. Huang, S. Gu, J.X. Jiang, Age-related deterioration of bone toughness is related to diminishing amount of matrix glycosaminoglycans (GAGs), JBMR Plus 2 (2018) 164–173, https://doi.org/10.1002/jbm4.10030.
[14] R. Hua, J.X. Jiang, Small leucine-rich proteoglycans in physiological and biomechanical function of bone, Matrix Biology Plus 11 (2021), https://doi.org/10.1016/j.mbplus.2021.100063 100063.
[15] Y. Han, J. Gomez, R. Hua, P. Xiao, W. Gao, J.X. Jiang, X. Wang, Removal of glycosaminoglycans affects the in situ mechanical behavior of extrafibrillar matrix in bone, J. Mech. Behav. Biomed. Mater. 123 (2021), https://doi.org/10.1016/j.jmbbm.2021.104766 104766.
[16] J.S. Nyman, A. Roy, X. Shen, R.L. Acuna, J.H. Tyler, X. Wang, The influence of water removal on the strength and toughness of cortical bone, J. Biomech. 39 (2006) 931–938, https://doi.org/10.1016/j.jbiomech.2005.01.012.
[17] M.A. Fernández, S.L. Wehrli, F.W. Wehrli, Diffusion of exchangeable water in cortical bone studied by nuclear magnetic resonance, Biophys. J. 82 (2002) 522–529, https://doi.org/10.1016/S00063495(02)75417-9.
[18] M. Granke, M.D. Does, J.S. Nyman, The role of water compartments in the material properties of cortical bone, Calcif. Tissue Int. 97 (2015) 292–307, https://doi.org/10.1007/s00223-015-9977-5.
[19] P. Timmins, J. Wall, Bone water, Calcif. Tissue Res. 23 (1997) 1–5, https://doi.org/10.1007/BF02012759.
[20] R. Ailavajhala, W. Querido, C.S. Rajapakse, N. Pleshko, Near infrared spectroscopic assessment of loosely and tightly bound cortical bone water, Analyst 145 (2020) 3713–3724, https://doi.org/10.1039/C9AN02491C.
[21] D. Zhang, S. Weinbaum, S. Cowin, Estimates of the peak pressures in bone pore water, J. Biomech. Eng. 120 (1998) 697–703, https://doi.org/10.1115/1.2834881.
[22] S. Nomura, A. Hiltner, J.B. Lando, E. Baer, Interaction of water with native collagen, Biopolymers 16 (1977) 231–246, https://doi.org/10.1002/bip.1977.360160202.
[23] M.H. Pineri, M. Escoubes, G. Roche, Water–collagen interactions: calorimetric and mechanical experiments, Biopolymers 17 (1978) 2799–2815, https://doi.org/10.1002/bip.1978.360171205.
[24] Q. Ni, H. Leng, D. P. Nicolella, The assessment of loosely and tightly bound water in water distribution changes of human cortical bone by nmr, in: Proceedings of the ASME 2008 Summer Bioengineering Conference. ASME 2008 Summer Bioengineering Conference, Parts A and B, 2008, pp. 357–358, https://doi.org/10.1115/SBC2008-192571.
[25] W.F. Neuman, T.Y. Toribara, B.J. Mulryan, The surface chemistry of bone. VII. The hydration shell1, J. Am. Chem. Soc. 75 (1953) 4239–4242, https://doi.org/10.1021/ja01113a028.
[26] E.E. Wilson, A. Awonusi, M.D. Morris, D.H. Kohn, M.M. Tecklenburg, L.W. Beck, Highly ordered interstitial water observed in bone by nuclear magnetic resonance, J. Bone Miner. Res. 20 (2009), https://doi.org/10.1359/JBMR.041217.
[27] V.L. Ferguson, Deformation partitioning provides insight into elastic, plastic, and viscous contributions to bone material behavior, J. Mech. Behav. Biomed. Mater. 2 (2009) 364–374, https://doi.org/10.1016/j.jmbbm.2009.01.004.
[28] M.-L. Lau, K.-T. Lau, H. Ku, F. Cardona, J.-H. Lee, Analysis of heat-treated bovine cortical bone by thermal gravimetric and nanoindentation, Compos. B Eng. 55 (2013) 447–452, https://doi.org/10.1016/j.compositesb.2013.06.027.
[29] L.D. Mkukuma, J.M.S. Skakle, I.R. Gibson, C.T. Imrie, R.M. Aspden, D.W.L. Hukins, Effect of the proportion of organic material in bone on thermal decomposition of bone mineral: an investigation of a variety of bones from different species using thermogravimetric analysis coupled to mass spectrometry, high-temperature X-ray diffraction, and fourier transform infrared spectroscopy, Calcif. Tissue Int. 75 (2004) 321–328, https://doi.org/10.1007/s00223-004-0199-5.
[30] M. Unal, S. Yang, O. Akkus, Molecular spectroscopic identification of the water compartments in bone, Bone 67 (2014) 228–236, https://doi.org/10.1016/j.bone.2014.07.021.
[31] M.L. Knothe Tate, U. Knothe, An ex vivo model to study transport processes and fluid flow in loaded bone, J. Biomech. 33 (2000) 247–254, https://doi.org/10.1016/S0021-9290(99)00143-8.
[32] S. Weinbaum, S.C. Cowin, Y. Zeng, A model for the excitation of osteocytes by mechanical loading-induced bone fluid shear stresses, J. Biomech. 27 (1994) 339–360, https://doi.org/10.1016/0021-9290(94)90010-8.
[33] X. Zhou, J.E. Novotny, L. Wang, Modeling fluorescence recovery after photobleaching in loaded bone: potential applications in measuring fluid and solute transport in the osteocytic lacunar canalicular system, Ann. Biomed. Eng. 36 (2008) 1961–1977, https://doi.org/10.1007/s10439-008-9566-0.
[34] E.H. Burger, J. Klein-Nulend, Mechanotransduction in bone–role of the lacuno-canalicular network, FASEB J.: Official Publ. Federation Am. Soc. Exp. Biol. 13 (Suppl) (1999) S101–S112.
[35] S.C. Cowin, Mechanosensation and fluid transport in living bone, J. Musculoskeletal Neuronal Interactions 2 (2002) 256–260.
[36] S.P. Fritton, S. Weinbaum, Fluid and solute transport in bone: flowinduced mechanotransduction, Annu. Rev. Fluid Mech. 41 (2009) 347–374, https://doi.org/10.1146/annurev.fluid.010908.165136.
[37] A.G. Robling, A.B. Castillo, C.H. Turner, Biomechanical and molecular regulation of bone remodeling, Annu. Rev. Biomed. Eng. 8 (2006) 455–498, https://doi.org/10.1146/annurev.bioeng.8.061505.095721.
[38] R. Marsell, T.A. Einhorn, The biology of fracture healing, Injury 42 (2011) 551–555, https://doi.org/10.1016/j.injury.2011.03.031.
[39] A.E. Goodship, The law of bone remodelling, J. Anat. 155 (1987) 217.
[40] S.C. Cowin, Bone poroelasticity, J. Biomech. 32 (1999) 217–238, https://doi.org/10.1016/s0021-9290(98)00161-4.
[41] L. You, S.C. Cowin, M.B. Schaffler, S. Weinbaum, A model for strain amplification in the actin cytoskeleton of osteocytes due to fluid drag on pericellular matrix, J. Biomech. 34 (2001) 1375–1386, https://doi.org/10.1016/s0021-9290(01)00107-5.
[42] A.F. van Tol, V. Schemenz, W. Wagermaier, A. Roschger, H. Razi, I. Vitienes, P. Fratzl, B.M. Willie, R. Weinkamer, The mechanoresponse of bone is closely related to the osteocyte lacunocanalicular network architecture, Proc. Natl. Acad. Sci. U.S.A. 117 (51) (2020) 32251–32259, https://doi.org/10.1073/pnas.2011504117.
[43] B.R. McCreadie, S.J. Hollister, M.B. Schaffler, S.A. Goldstein, Osteocyte lacuna size and shape in women with and without osteoporotic fracture, J. Biomech. 37 (2004) 563–572, https://doi.org/10.1016/S00219290(03)00287-2.
[44] J.D. Currey, R. Shahar, Cavities in the compact bone in tetrapods and fish and their effect on mechanical properties, J. Struct. Biol. 183 (2013) 107–122, https://doi.org/10.1016/j.jsb.2013.04.012.
[45] R.R. Cooper, J.W. Milgram, R.A. Robinson, Morphology of the osteon. An electron microscopic study, J. Bone Joint Surgery Am. 48 (7) (1966) 1239–1271.
[46] C.-Y. Lin, C.-Y. Chiang, H.-J. Tsai, Zebrafish and Medaka: new model organisms for modern biomedical research, J. Biomed. Sci. 23 (2016) 19, https://doi.org/10.1186/s12929-016-0236-5.
[47] L. Ofer, P. Zaslansky, R. Shahar, A comparison of the structure, composition and mechanical properties of anosteocytic vertebrae of medaka (O. latipes) and osteocytic vertebrae of zebrafish (D. rerio), J. Fish Biol. 98 (2021) 995–1006, https://doi.org/10.1111/jfb.14334.
[48] L. Ofer, M.N. Dean, P. Zaslansky, S. Kult, Y. Shwartz, J. Zaretsky, S. Griess-Fishheimer, E. Monsonego-Ornan, E. Zelzer, R. Shahar, A novel nonosteocytic regulatory mechanism of bone modeling, PLoS Biol. 17 (2019) e3000140, https://doi.org/10.1371/journal.pbio.3000140.
[49] L. Ofer, M. Dumont, A. Rack, P. Zaslansky, R. Shahar, New insights into the process of osteogenesis of anosteocytic bone, Bone 125 (2019) 61–73, https://doi.org/10.1016/j.bone.2019.05.013.
[50] R. Shahar, M.N. Dean, The enigmas of bone without osteocytes, BoneKEy Reports 2 (2013) 343, https://doi.org/10.1038/bonekey.2013.77.
[51] M. Unal, O. Akkus, Raman spectral classification of mineraland collagen-bound water's associations to elastic and post-yield mechanical properties of cortical bone, Bone 81 (2015) 315–326, https://doi.org/10.1016/j.bone.2015.07.024.
[52] R. Ailavajhala, J. Oswald, C.S. Rajapakse, N. Pleshko, Environmentally-controlled near infrared spectroscopic imaging of bone water, Sci. Rep. 9 (2019) 10199, https://doi.org/10.1038/s41598019-45897-3.
[53] F.W. Wehrli, M.A. Fernández, Nuclear magnetic resonance studies of bone water, Ann. Biomed. Eng. 33 (2005) 79–86, https://doi.org/10.1007/s10439-005-8965-8.
[54] H.H. Ong, A.C. Wright, F.W. Wehrli, Deuterium nuclear magnetic resonance unambiguously quantifies pore and collagen-bound water in cortical bone, J. Bone Miner. Res. 27 (2012) 2573–2581, https://doi.org/10.1002/jbmr.1709.
[55] B. Schillinger, E. Lehmann, P. Vontobel, 3D neutron computed tomography: requirements and applications, Physica B 276–278 (2000) 59–62, https://doi.org/10.1016/S0921-4526(99)01254-5.
[56] C. Tötzke, N. Kardjilov, I. Manke, S.E. Oswald, Capturing 3D water flow in rooted soil by ultra-fast neutron tomography, Sci. Rep. 7 (2017) 6192, https://doi.org/10.1038/s41598-017-06046-w.

[57] E. Tudisco, M. Etxegarai, S.A. Hall, E.M. Charalampidou, G.D. Couples, H. Lewis, A. Tengattini, N. Kardjilov, Fast 4-D imaging of fluid flow in rock by high-speed neutron tomography, J. Geophys. Res. (Solid Earth) 124 (2019) 3557–3569, https://doi.org/10.1029/2018JB016522.
[58] F. Guillaume, S.L. Cann, A. Tengattini, E. Törnquist, C. FalentinDaudre, H.A. Lomami, Y. Petit, H. Isaksson, G. Ha¨ıat, Neutron microtomography to investigate the bone-implant interface—comparison with histological analysis, Phys. Med. Biol. 66 (2021) 105006, doi: 10.1088/1361-6560/abf603.
[59] N. Kardjilov, A. Hilger, I. Manke, R. Woracek, J. Banhart, CONRAD-2: the new neutron imaging instrument at the Helmholtz-Zentrum Berlin, J. Appl. Crystallogr. 49 (2016), https://doi.org/10.1107/S1600576715023353.
[60] S. Flenner, M. Storm, A. Kubec, E. Longo, F. Döring, D.M. Pelt, C. David, M. Müller, I. Greving, Pushing the temporal resolution in absorption and Zernike phase contrast nanotomography: enabling fast in situ experiments, Journal of Synchrotron Radiation 27 (2020) 1339–1346, https://doi.org/10.1107/S1600577520007407.
[61] R.B. Myers, J.L. Fredenburgh, W.E. Grizzle, 11 - Carbohydrates, in: J.D. Bancroft, M. Gamble (Eds.), Theory and Practice of Histological Techniques, sixth ed., Churchill Livingstone, Edinburgh, 2008, pp. 161–186, https://doi.org/10.1016/B978-0-443-10279-0.50018-X.
[62] S. Suniaga, T. Rolvien, A. vom Scheidt, I.A.K. Fiedler, H.A. Bale, A. Huysseune, P. E. Witten, M. Amling, B. Busse, Increased mechanical loading through controlled swimming exercise induces bone formation and mineralization in adult zebrafish, Sci. Rep. 8 (2018) 3646, https://doi.org/10.1038/s41598-018-21776-1.
[63] S. Gamsjaeger, K. Klaushofer, E.P. Paschalis, Raman analysis of proteoglycans simultaneously in bone and cartilage, J. Raman Spectrosc. 45 (2014) 794–800, https://doi.org/10.1002/jrs.4552.
[64] S. Das Gupta, M.A.J. Finnilä, S.S. Karhula, S. Kauppinen, A. Joukainen, H. Kröger, R.K. Korhonen, A. Thambyah, L. Rieppo, S. Saarakkala, Raman microspectroscopic analysis of the tissuespecific composition of the human osteochondral junction in osteoarthritis: a pilot study, Acta Biomater. 106 (2020) 145–155, https://doi.org/10.1016/j.actbio.2020.02.020.
[65] G. Quintarelli, J.E. Scott, M.C. Dellovo, The chemical and histochemical properties of Alcian Blue. II. Dye binding of tissue polyanions, Histochem. Histochem. Histochimie 4 (1964) 86–98, https://doi.org/10.1007/BF00306150.
[66] J.L. Hyllested, K. Veje, K. Ostergaard, Histochemical studies of the extracellular matrix of human articular cartilage—a review, Osteoarthritis Cartilage 10 (2002) 333–343, https://doi.org/10.1053/joca.2002.0519.
[67] T.M. Skerry, R. Suswillo, A.J. el Haj, N.N. Ali, R.A. Dodds, L.E. Lanyon, Load-induced proteoglycan orientation in bone tissue in vivo and in vitro, Calcif. Tissue Int. 46 (1990) 318–326, https://doi.org/10.1007/BF02563823.
[68] B. Yu, A. Pacureanu, C. Olivier, P. Cloetens, F. Peyrin, Assessment of the human bone lacuno-canalicular network at the nanoscale and impact of spatial resolution, Sci. Rep. 10 (2020) 4567, https://doi.org/10.1038/s41598-020-61269-8.
[69] P.E. Palacio-Mancheno, A.I. Larriera, S.B. Doty, L. Cardoso, S.P. Fritton, 3D Assessment of cortical bone porosity and tissue mineral density using high-resolution micro-CT: effects of resolution and threshold method, J. Bone Mineral Res.: Official J. Am. Soc. Bone Mineral Res. 29 (2014). doi: 10.1002/jbmr.2012.10.1002/jbmr.2012.
[70] S.M. Tommasini, A. Trinward, A.S. Acerbo, F. De Carlo, L.M. Miller, S. Judex, Changes in intracortical microporosities induced by pharmaceutical treatment of osteoporosis as detected by high resolution microCT, Bone 50 (2012) 596–604, https://doi.org/10.1016/j.bone.2011.12.012.
[71] G.S. Mandair, M.D. Morris, Contributions of Raman spectroscopy to the understanding of bone strength, BoneKEy Reports 4 (2015) 620, https://doi.org/10.1038/bonekey.2014.115.
[72] L. Wang, C. Ciani, S.B. Doty, S.P. Fritton, Delineating bone's interstitial fluid pathway in vivo, Bone 34 (2004) 499–509, https://doi.org/10.1016/j.bone.2003.11.022.
[73] F. Yang, W. Yu, X. Huo, H. Li, Q. Qi, X. Yang, N. Shi, X. Wu, W. Chen, Effects of osteocyte shape on fluid flow and fluid shear stress of the loaded bone, Biomed Res. Int. 2022 (2022) 3935803, https://doi.org/10.1155/2022/3935803.
[74] L. Cardoso, S.P. Fritton, G. Gailani, M. Benalla, S.C. Cowin, Advances in assessment of bone porosity, permeability and interstitial fluid flow, J. Biomech. 46 (2013) 253–265, https://doi.org/10.1016/j.jbiomech.2012.10.025.
[75] G. Gailani, M. Benalla, R. Mahamud, S.C. Cowin, L. Cardoso, Experimental determination of the permeability in the lacunar-canalicular porosity of bone, J. Biomech. Eng. 131 (2009) 101007, https://doi.org/10.1115/1.3200908.
[76] S. Reitsma, D.W. Slaaf, H. Vink, M.A.M.J. van Zandvoort, M.G.A. oude Egbrink, The endothelial glycocalyx: composition, functions, and visualization, Pflu¨gers Archiv – Eur. J. Physiolhttps://doi.org/10.1007/s00424-007-0212-8. 454 (2007) 345–359, .
[77] N. Nijenhuis, D. Mizuno, J.A.E. Spaan, C.F. Schmidt, Viscoelastic response of a model endothelial glycocalyx, Phys. Biol. 6 (2009), https://doi.org/10.1088/1478-3975/6/2/025014 025014.
[78] J.M. Tarbell, Z.-D. Shi, Effect of the glycocalyx layer on transmission of interstitial flow shear stress to embedded cells, Biomech. Model. Mechanobiol. 12 (2013) 111–121, https://doi.org/10.1007/s10237-012-0385- 8.
[79] T. Lemaire, S. Näıli, A. Rémond, Study of the influence of fibrous pericellular matrix in the cortical interstitial fluid movement with hydroelectrochemical effects, J. Biomech. Eng. 130 (2008), https://doi.org/10.1115/1.2838025 011001.
[80] Y. Yokoyama, Y. Kameo, H. Kamioka, T. Adachi, High-resolution image-based simulation reveals membrane strain concentration on osteocyte processes caused by tethering elements, Biomech. Model. Mechanobiol. 20 (2021) 2353–2360, https://doi.org/10.1007/s10237-02101511-y.
[81] L.-D. You, S. Weinbaum, S.C. Cowin, M.B. Schaffler, Ultrastructure of the osteocyte process and its pericellular matrix, Anatomical Record Part A Discoveries Mol. Cellular Evol. Biol. 278 (2004) 505–513, https://doi.org/10.1002/ar.a.20050.
[82] E. Törnquist, S. Le Cann, A. Tengattini, L. Helfen, J. Kok, S.A. Hall, H. Isaksson, The hydration state of bone tissue affects contrast in neutron tomographic images, Front. Bioeng. Biotechnol. 10 (2022), https://doi.org/10.3389/fbioe.2022.911866 911866.
[83] E. Törnquist, S. Le Cann, E. Tudisco, A. Tengattini, E. And, N. Lenoir, J. Hektor, D. B. Raina, M. Ta¨gil, S. A. Hall, H. Isaksson, Dual modality neutron and x-ray tomography for enhanced image analysis of the bone-metal interface, Phys. Med. Biol. 66 (2021), https://doi.org/10.1088/1361-6560/ac02d4.
[84] M.A. Fernández, S.L. Wehrli, M. Takahashi, F.W. Wehrli, Water content measured by proton-deuteron exchange NMR predicts bone mineral density and mechanical properties, J. Bone Miner. Res. 19 (2004) 289–296, https://doi.org/10.1359/JBMR.0301227.
[85] R. Nanda, S. Hazan, K. Sauer, V. Aladin, K. Keinan-Adamsky, B. Corzilius, R. Shahar, P. Zaslansky, G. Goobes, Molecular differences in collagen organization and in organic-inorganic interfacial structure of bones with and without osteocytes, Acta Biomater. 144 (2022) 195–209, https://doi.org/10.1016/j.actbio.2022.03.032.
[86] N. Tiwari, R. Rai, N. Sinha, Water-lipid interactions in native bone by high-resolution solid-state NMR spectroscopy, Solid State Nucl. Magn. Reson. 107 (2020), https://doi.org/10.1016/j.ssnmr.2020.101666 101666.
[87] B.A. Dowd, G.H. Campbell, R.B. Marr, V.V. Nagarkar, L.A. Tipnis, D.P. Siddons, Developments in synchrotron x-ray computed microtomography at the National Synchrotron Light Source, Proc. SPIE 3772, Developments in X-Ray Tomography II 3772 (1999) 224–236, https://doi.org/10.1117/12.363725.
[88] G. Doga, F. De Carlo, X. Xiao, C. Jacobsen, TomoPy: A framework for the analysis of synchrotron tomographic data, Journal of Synchrotron Radiation 21 (2014) 1188–1193, https://doi.org/10.1107/S1600577514013939.